GSA Data Repository 2020106 https://doi.org/10.1130/G46650.1

SUPPLEMENTARY MATERIALS FOR:

Direct evidence for fluid overpressure during hydrocarbon generation and expulsion from organic-rich shales

Miao Wang[1, 2], Yong Chen[1, 3]*, Wyatt M. Bain[2], Guoqi Song[1], Keyu Liu[1], Zhenzhu Zhou[3] and Matthew Steele-MacInnis[2]

[1]*School of Geosciences, China University of Petroleum (East China), Qingdao, Shandong, 266580, China*

[2]*Dept. of Earth & Atmospheric Sciences, University of Alberta, Edmonton, Alberta, T6G2E3, Canada*

[3]*Shandong Key Lab. of Depositional Mineralization & Sedimentary Mineral, Shandong University of Science & Technology, Qingdao, Shandong, 266590, China*

ADDITIONAL DETAILS ON METHODS

Micro-spectrofluorimetry analysis

Fluid inclusion petrographic analysis carried out by using a Leica DM-2700P microscope with transmitted light (TL) and ultra-violet (UV) illumination (365 nm peak of Hg). The wavelength of excitation filter used for the fluorescence is from 340 – 380 nm, and of suppression filter is 425 nm. Micro-spectrofluorimetry was used to study the liquid hydrocarbon phase of individual inclusions under ultra-violet illumination, using a TIDAS MSP 400 miniature fibre optic spectrometer. Parameters λ_{max} (wavelength of maximum intensity), $Q_{(650/500)}$ (the ratio of the intensity at 650 nm to the intensity at 500 nm) and Q_{F-535}

(the ratio of the 535 – 750 nm flux to the 430 – 535 nm flux) were used to determine the gross compositions of liquid hydrocarbons of entrapped oil and their maturity.

Laser Raman spectroscopic analysis

Raman spectroscopy of organic matter can be used as an indicator of the thermal maturity. Laser Raman analyses of the median plane and primary bitumen inclusions in BDPVs were performed on a Bruker SENTERRA spectrometer and a 532 nm Ar-ion laser focused to a 1 μm spot through a 100x objective mounted on a petrographic microscope at MacEwan University (Edmonton, AB). All spectra were acquired using a laser power of 20 mW and two to three, 5-10s exposures summed to the final reported spectra. A silicon wafer was used for wavenumber calibration. The Raman spectra were acquired and processed by using the LabSpec 5 software by HORIBA. Linear baseline subtraction was performed on a spectra truncated between 1100 and 1800 cm^{-1} (Fig. DR1A). Following this processing, D1-, D2-, D3-, D4- and G-bands (Fig. DR1B) were fitted by a decomposition using Gaussian-Lorentzian peak shapes, following the procedure described by Sforna et al. (2014). Peak positions, intensities, areas and widths of each band was recorded. Raman spectra have been widely used as proxies to estimate the peak temperatures and thermal maturities experienced by organic matter (Liu et al., 2013; Wilkins et al., 2014; Kouketsu et al., 2014; Schito et al., 2017). In light of the known geological context of our study area, we applied the thermometer established by Kouketsu et al. (2014) based on full width at half maximum of D1-band (FWHM-D1, Eq. 1). Previous testing by Baludikay et al. (2018) has shown that this empirical model provides the best performance for the conditions of diagenesis (i.e., < 200 °C).

$$T\ (°C) = -2.15 * FWHM\text{-}D1+478. \quad (1)$$

Microthermometry of fluid inclusions

Microthermometric studies of fluid inclusions were carried out by using a Linkam THMSG600 heating-cooling stage with temperature calibrated according to the triple point of H_2O (0.0 °C) and the critical point of H_2O (374.1 °C) using synthetic pure H_2O fluid inclusion, and the triple point of CO_2 (-56.6 °C) using synthetic CO_2 fluid inclusions. For the inclusions measured here, we always conducted the heating measurements (analysis of homogenization temperature, T_h) prior to cooling the samples, because the volume fraction of vapor in the aqueous inclusions was small and freezing could have induced stretching, which would affect the measured T_h. Thus, by heating prior to cooling, we were able to confidently measure unmodified T_h, and determine salinity thereafter by subsequent freezing. During heating from room temperature, both the two-phase hydrocarbon and aqueous inclusions homogenized to liquid. The homogenization temperatures of fluid inclusions in each FIA were obtained by thermal cycling using temperature steps of 1°C as described by Goldstein and Reynolds (1994). For the monophase hydrocarbon inclusions, all inclusions nucleated a gas bubble when temperature reached approximately -60 °C during cooling. After nucleation, the inclusions were re-heated to measure the homogenization temperature. Final ice melting temperatures of aqueous inclusions were obtained after freezing using temperature steps of 1°C. The precision of the microthermometry is estimated to be ±0.1°C over the entire temperature range.

PVT modeling

The compositions of the petroleum inclusions were acquired on populations of inclusions by crushing the samples, and analyzing the resulting leachates by chromatography and mass spectrometry (Table DR1). The volume fraction of vapor of the two-phase hydrocarbon inclusions at room temperature were estimated by optical microscopy as described by Roedder (1984), and by digital image analysis. Only the inclusions with regular and equilateral shapes were selected for estimation of the volume fraction of vapor.

The thermodynamic calculations of fluid phase equilibria and isochore for hydrocarbon inclusions was done using the Peng-Robinson equation of state as implemented in the computer program *PVTsim*. The input parameters in these calculations were 1) the hydrocarbon compositions acquired on populations by crush/leach analysis, and 2) the homogenization temperatures of the 5 samples. In these calculations, we followed the method of Aplin et al. (1999). Specifically, we used the *PVTsim* software to calculate the saturation pressure at the homogenization temperature of the inclusion, and then calculated the total molar volume at the pressure-temperature point of homogenization. The calculated (theoretical) volume fraction of vapor at room temperature was obtained by calculating the conditions at which the molar volume of the mixture at room temperature matched the molar volume calculated at the homogenization temperature. Thus, the representativeness (accuracy) of the measured petroleum composition (measured based on populations, and now compared to the petroleum composition within each individual inclusion) was verified by comparison of the calculated volume fraction of vapor and the measured values obtained by optical microscopy and image analysis.

Methane is the most soluble hydrocarbon component in the aqueous phase coexisting with oil phase, and even minor concentrations of CH_4 in the aqueous inclusions can greatly influence PVT interpretation (Dubessy et al., 2001; Caumon et al., 2014). However, as described below, no CH_4 was detected in the aqueous inclusions by Raman analysis (Fig. DR4). Hence the PVT properties of the aqueous inclusions were modeled based on the H_2O-NaCl system. The thermodynamic calculations of phase equilibria and isochore of the aqueous inclusions were based on the model of Steele-MacInnis et al. (2012), with input parameters of ice melting temperatures and the homogenization temperatures. To determine the trapping pressure, we used the approach of intersecting isochores of coexisting petroleum and aqueous inclusions (Goldstein, 2001).

Basin modeling

Basin modeling of Well NY-1 was conducted using the *Basinmod 1D* software. Input parameters in this modeling were: the strata top depth; stratigraphic present thickness; absolute ages; lithology; missing erosional thickness; surface temperature; measured borehole temperatures (BHT); and heat flux during each stage. Modeling based on these parameters was done to generate the standard burial history of the well. A summary of the information upon which this parameterization was based is as follows.

The Bohai Bay Basin is located in East China (Fig. 1A), and represents a faulted-depressed basin developed in the Paleozoic cratonic basement, filled by Mesozoic-Cenozoic strata. The Cenozoic strata of the Dongying Depression comprise the Eocene Kongdian Formation (Ek), Eocene Shahejie Formation (Es), Eocene Dongying Formation (Ed), Neogene Guantao Formation (Ng), Neogene Minghuazhen Formation (Nm) and the Quaternary Pingyuan Formation (Qp), respectively from bottom to top (Fig. 1B). The tectonic evolution of the basin consists of the syn-rifting stage (65.0-24.6 Ma, during the deposition stage of the Kongdian, Shahejie and Dongying Formations) and post-rifting stage (24.6 Ma to the present, during the deposition stage of Guantao, Minghuazhen and Pingyuan Formations). The syn-rifting stage occurred from the Palaeocene to the Oligocene and can be subdivided into 4 episodes including an initial episode (I), an expansion episode (II), an expansion and rapid subsiding episode (III), and a contraction episode (IV) (Chang, 1991; Xie et al., 2001). A subsequent period of uplift and erosion followed the deposition of the Dongying Formation from 24.6 to 14 Ma, and the contact with the overlying Guantao Formation is a regional unconformity in the study area (Guo et al., 2014).

The data we used for the basin modelling are presented in the Table DR4. The input information about the strata top depth, the present thickness, the lithology and the missing erosional thickness of the Well NY-1 was acquired from the well log profile from Shengli Oil Company, SINOPEC. The current heat flux was calculated based on the measured BHT, with the result of 67.3 mW/m^2, using the transient heat flux model in the software. The values of the paleo heat flux during the deposition of each formation were from Guo et al. (2012) and Qiu et al. (2014) in the Bohai Bay Basin, from which a good agreement between the measured and calculated Ro and temperature has been verified. An average surface temperature was set at 15 °C for the entire geological time in the modelling (Guo et al., 2012; Qiu et al., 2014). The initial porosity, matrix density, matrix thermal conductivity and matrix heat capacity were adopted from the default values in the *Basinmod 1D* software.

After completion of the basin model, the time dependent litho- and hydro-static regimes of the five samples were then deduced from the basin model following the procedures outlined by Bourdet et al. (2010) and Renard et al. (2019). The modelling provides a reconstruction of the pressure-temperature-time trajectory under both hydrostatic and lithostatic regimes throughout the basin evolution. The resulting trajectory in PT space is related to the evolving heat flow, sedimentation and compaction rates through time. Combined with the fluid inclusion data plotted in the same graph, this provides an assessment of the relationship between fluid pressure versus hydrostatic and lithostatic pressures at the time when the fluid inclusions were trapped (Fig. 4 and DR5).

ADDITIONAL DETAILS ON RESULTS

The two-phase hydrocarbon inclusions consist of both a hydrocarbon liquid phase with various UV-fluorescence colors (yellow, yellow-green, green) and a non-luminescent hydrocarbon gas phase (Figs. DR2). The inclusions in any individual FIA show consistent fluorescence colors. In most cases fluorescence of petroleum is used to give a fingerprint of the composition of hydrocarbons and different fluorescence colors indicate variable compositions and maturities of the oil inclusions. Thus, the parameters deduced from the micro-spectrofluorimetry are very sensitive to the chemical compositions and API (American Petroleum Institute) gravity of hydrocarbon in inclusions (Stasiuk and Snowdon, 1997; Bourdet et al., 2014; Nandakumar and Jayanthi, 2016). As for the micro-spectrofluorimetry results, the yellow fluorescence color have relatively high value of λ_{max} (avg. = 568 nm), $Q_{(650/500)}$ (avg. = 0.71) and Q_{F-535} (avg. = 1.99), the yellow-green fluorescence colors exhibit lower λ_{max} (avg. = 536 nm), $Q_{(650/500)}$ (avg. = 0.51) and $Q_{F\text{-}535}$ (avg. = 1.38), while the green fluorescence colors show the lowest λ_{max} (avg. = 511 nm), $Q_{(650/500)}$ (avg. = 0.39) and $Q_{F\text{-}535}$ (avg. = 1.09) (Fig. DR2; Table DR2). From yellow to green fluorescence, the heavy components (heterocompounds and aromatic hydrocarbons fraction) decrease, whereas the light components (saturated hydrocarbons fraction) increase with the green fluorescent color indicative of relatively high maturity (Hagemann and Hollerbach, 1986; Munz, 2000). In addition, the spectral shape (Fig. DR2) and the fluorescence parameters (Table DR2) of the individual petroleum inclusions that make up a given FIA are very consistent along the direction of the fiber growth. Thus, the gross degree of maturity of the hydrocarbon fluids in these veins is relatively low, and the liquid hydrocarbon composition remained consistent during the BPFVs growth.

Two types of bitumen-bearing inclusions are present in veins. The first is characterized by bitumen which coats the wall of the inclusions with the weak fluorescence intensity (Fig. 3A). The second type coexists with petroleum inclusions within the same FIAs and is difficult to differentiate from monophase aqueous inclusions, based solely on petrography. However, Raman spectra of this second type of inclusions show a strong feature at around 1600 cm^{-1} and a weaker feature at around 1360 cm^{-1} (Fig. 3B), which indicates that these are bitumen inclusions. The formation temperatures of these primary monophase bitumen inclusions based on Raman geothermometers range from 133.2 to 157.2 °C (avg. = 145.7 °C), which generally overlap with, but extend to slight higher values than the median planes (130.6 to 141.0 °C; avg. = 133.6 °C; Table DR3). This generally suggests that, from the median plane to the vein wall (i.e., along the direction of antitaxial growth) in BPFVs, the temperatures were rising due to the increasing burial depth during the hydrocarbon generation and expulsion from organic-rich shales.

Verification of the representativeness of the (bulk) composition data used for the thermodynamic calculations of the two-phase hydrocarbon inclusions was as follows. The estimated volume fractions of vapor of the selected hydrocarbon inclusions in five samples, based on optical microscopy and image analysis, were from 5 to 10%. The values obtained from the thermodynamic calculations of the five samples, from shallow to deep, were 7.7-10.2%, 6.8-9.4%, 7.4-9.1%, 6.9-11.8% and 7.4-9.4%, respectively. Thus, the calculated volume fractions of vapor at room temperature matched the estimated values, suggesting the petroleum composition data acquired on populations of inclusions in the five samples are accurate representations of the petroleum within the individual inclusions in each sample. In addition, as we mentioned above, the HIs within any individual FIA show consistent fluorescence colors and nearly uniform micro-spectrofluorimetry parameters, which also indicate that the chemical compositions of the HIs are uniform within each FIA during the fiber growth.

DATA REPOSITORY REFERENCES CITED

Baludikay, B. K., François, C., Sforna, M. C., Beghin, J., Cornet, Y., Storme, J. Y., Fagel, N., Fontaine, F., Littke, Ralph., Daniel, B., Delvaux, D., and Javaux, D., 2018, Raman microspectroscopy, bitumen reflectance and illite crystallinity scale: comparison of different geothermometry methods on fossiliferous Proterozoic sedimentary basins (DR

Congo, Mauritania and Australia): International Journal of Coal Geology, v. 191, p. 80–94.

Bourdet, J., Burruss, R. C., Chou, I. M., Kempton, R., Liu, K., and Hung, N. V., 2014, Evidence for a palaeo-oil column and alteration of residual oil in a gas-condensate field: Integrated oil inclusion and experimental results: Geochimica et Cosmochimica Acta, v. 142. p, 362–385.

Chang, C. Y., 1991, Geological characteristics and distribution patterns of hydrocarbon deposits in the Bohai Bay Basin, east China: Marine and Petroleum Geology, v. 8, p. 98–106.

Guo, X., Liu, K., He, S., Song, G., Wang, Y., Hao, X., and Wang, B., 2012, Petroleum generation and charge history of the northern Dongying Depression, Bohai Bay Basin, China: insight from integrated fluid inclusion analysis and basin modelling: Marine and Petroleum Geology, v. 32, p. 21–35.

Guo, X., He, S., Liu, K., Song, G., Wang, X., and Shi, Z., 2010, Oil generation as the dominant overpressure mechanism in the Cenozoic Dongying depression, Bohai Bay Basin, China: AAPG Bulletin, v. 94, p. 1859–1881.

Hagemann, H. W., and Hollerbach, A., 1986, The fluorescence behaviour of crude oils with respect to their thermal maturation and degradation: Organic Geochemistry, v. 10, p. 473–480.

Liu, D., Xiao, X., Tian, H., Min, Y., Zhou, Q., Cheng, P., and Shen, J., 2013, Sample maturation calculated using Raman spectroscopic parameters for solid organics:

Methodology and geological applications: Chinese Science Bulletin, v. 58, p. 1285–1298.

Munz, I.A., 2001, Petroleum inclusions in sedimentary basins: systematics, analytical methods and applications: Lithos, v. 55, p. 195–212.

Nandakumar, V., and Jayanthi, J. L., 2016, Hydrocarbon fluid inclusions, API gravity of oil, signature fluorescence emissions and emission ratios: an example from Mumbai offshore, India: Energy & Fuels, v. 30, p. 3776–3782.

Qiu, N., Zuo, Y., Chang, J., and Li, W., 2014, Geothermal evidence of Meso-Cenozoic lithosphere thinning in the Jiyang sub-basin, Bohai Bay Basin, eastern North China Craton: Gondwana Research, v. 26, p. 1079–1092.

Roedder E., 1984, Fluid Inclusions. Mineralogical Society of America: v. 12.

Schito, A., Romano, C., Corrado, S., Grigo, D., and Poe, B., 2017, Diagenetic thermal evolution of organic matter by Raman spectroscopy: Organic Geochemistry, v. 106, p. 57–67.

Sforna, M. C., Van Zuilen, M. A., and Philippot, P., 2014, Structural characterization by Raman hyperspectral mapping of organic carbon in the 3.46 billion-year-old Apex chert, Western Australia: Geochimica et Cosmochimica Acta, v. 124, p. 18–33.

Stasiuk, L. D., and Snowdon, L. R., 1997, Fluorescence micro-spectrometry of synthetic and natural hydrocarbon fluid inclusions: crude oil chemistry, density and application to petroleum migration: Applied Geochemistry, v. 12, p. 229–241.

Wilkins, R. W., Boudou, R., Sherwood, N., and Xiao, X., 2014, Thermal maturity evaluation from inertinites by Raman spectroscopy: the 'RaMM' technique: International Journal of Coal Geology, v. 128, p. 143–152.

Xie, X., Bethke, C. M., Li, S., Liu, X., and Zheng, H., 2001, Overpressure and petroleum generation and accumulation in the Dongying Depression of the Bohaiwan Basin, China: Geofluids, v. 1, p. 257–271.

DATA REPOSITORY FIGURES

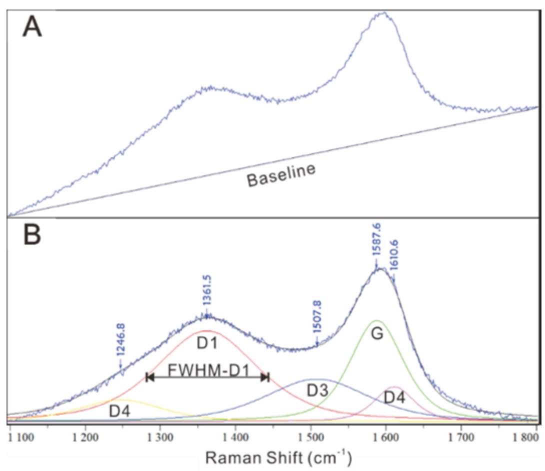

Figure DR1. A: Baseline subtraction of the Raman spectra of bitumen using a third order polynomial curve fit. B: Decomposition of the Raman spectra of bitumen. FWHM-D1 = full widths at half mean for a D1-band.

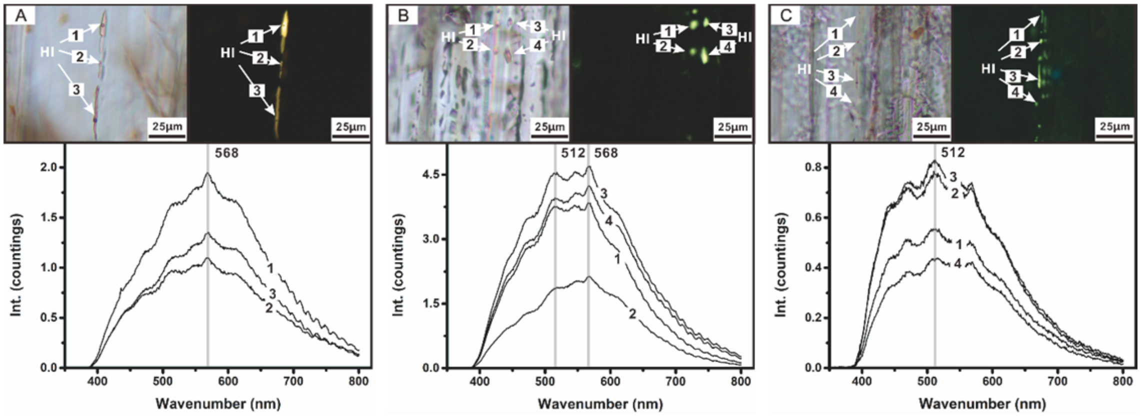

Figure DR2. Fluid inclusions hosted in BPFVs of Well NY-1 and micro-spectrofluorimetry. HI = Hydrocarbon inclusion. A: From 3296.0 m, hydrocarbon inclusions in one FIA showing yellow fluorescence color and their micro-spectrofluorimetry features. B: From 3432.0 m, hydrocarbon inclusions in one FIA showing yellow-green fluorescence color and their micro-spectrofluorimetry features. C: From 3426.0 m, hydrocarbon inclusions in one FIA showing green fluorescence color and their micro-spectrofluorimetry features.

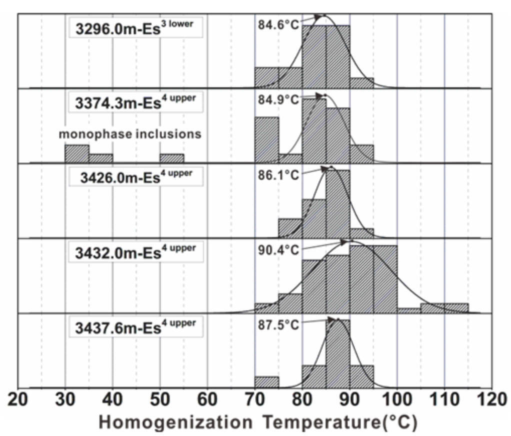

Figure DR3. Distribution histogram and Gaussian fit of hydrocarbon inclusions homogenization temperatures in BPFVs of 5 different burial-depths.

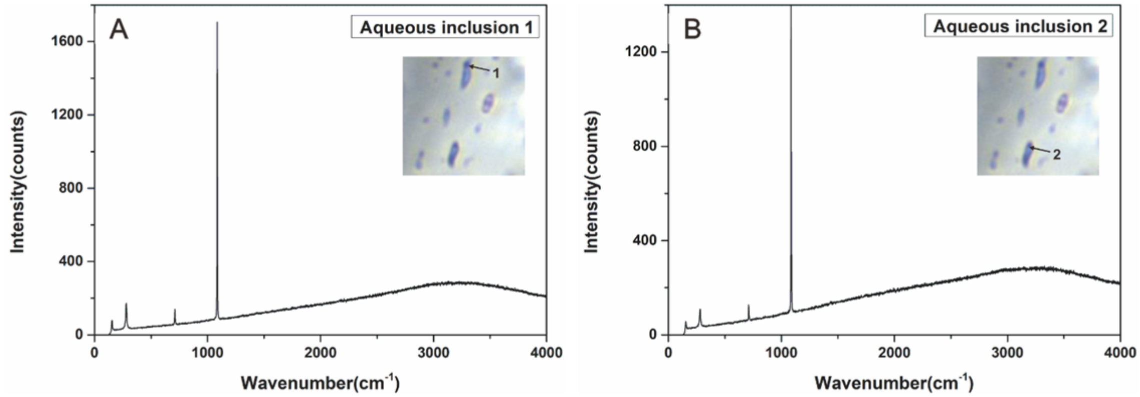

Figure DR4. Raman spectra of vapor phase within two-phase aqueous inclusions in the sample of 3432.0 m.

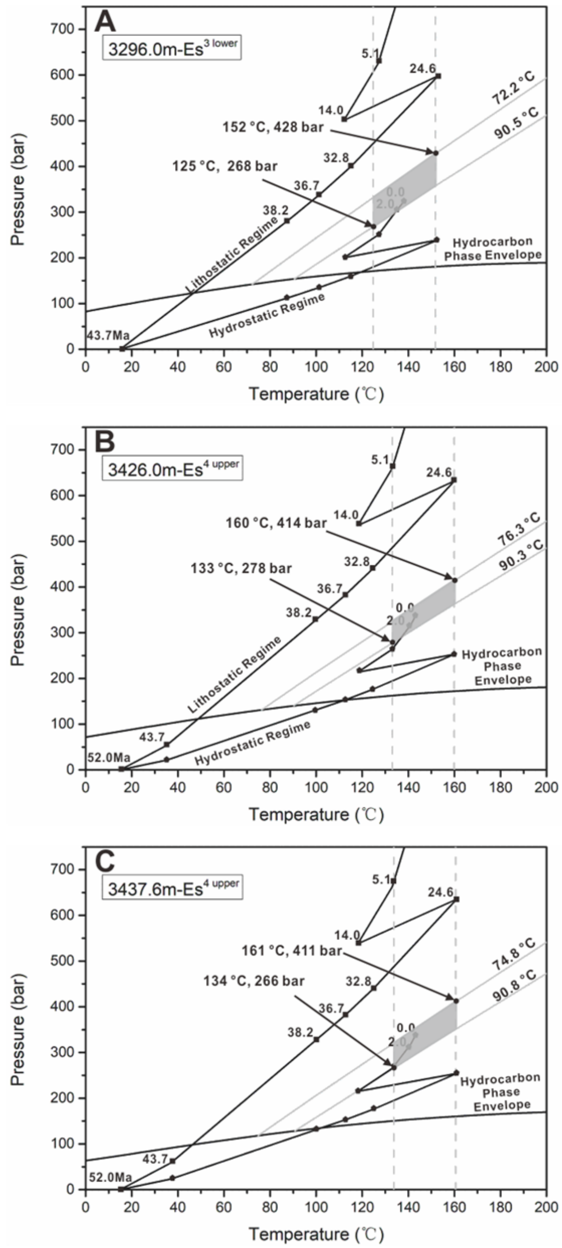

Figure DR5. P-T diagram showing intersecting isochore of two-phase hydrocarbon inclusions with the inferred trapping temperatures based on the burial history. The shaded area illustrates the proposed entrapment conditions of the fluid inclusions during the BPFV formation. A: From 3296.0 m. B: From 3426.0 m. C: From 3437.6 m.

DATA REPOSITORY TABLES

Table DR1. Hydrocarbon compositions of the five samples of Well NY-1

Compositions (mol. %)	**3296.0 (m)**	**3374.3 (m)**	**3426.0 (m)**	**3432.0 (m)**	**3437.6 (m)**
C_1	45.1	38.6	40.8	35.3	36.2
C_2	11.4	16.1	17.3	21.4	18.5
C_3	7.3	8.2	6.8	8.6	10.2
C_4	4.0	3.9	3.1	3.4	4.0
C_5	1.6	1.8	1.3	1.0	1.0
C_6	0.4	0.9	0.6	0.3	0.2
C_{7+}	30.1	30.4	30.2	30.1	30.0

Table DR2. Homogenization temperature values and micro-spectrofluorimetry parameters of the inclusions in BPFVs of Well NY-1

Depth (m)	**FIA**	**Type**	**Fluorescence Colour**	**T_h/T_m (°C)**	**λ_{max}**	**Q (650/500)**	**Q_{F-535}**
3296	1	FI	Yell.	82.8	568	0.85	1.99
	2	FI	Yell.	77.2			
		FI	Yell.	83.5			
	3	FI	Yell.	72.2			
		FI	Yell.	79.1	568	0.83	2.06
		FI	Yell.	81.3	567	0.82	1.98
		FI	Yell.	85.6	569	0.81	2.08
		FI	Yell.	74.9			
	4	FI	Yell.-Gre.	86	566	0.49	1.42
		FI	Yell.-Gre.	86.5			
		FI	Yell.-Gre.	86.5			
		FI	Yell.-Gre.	87.5			
		FI	Yell.-Gre.	83.9			
		FI	Yell.-Gre.	84.4			
		FI	Yell.-Gre.	89			
		FI	Yell.-Gre.	90.5			
		FI	Yell.-Gre.	84.3			
3374.3	1	FI	Yell.	88.1			
		FI	Yell.	90.3	568	0.80	1.82
		FI	Yell.	86.1			
		FI	Yell.	90.6			
		FI	Yell.	86.1			
		FI	Yell.	89.8			
	2	FI	Yell.	74.9			
		FI	Gre.	74.9			
	3	FI	Yell.	80.9			

		FI	Yell.	84.5	568	0.88	2.17
		FI	Yell.	84.5			
		FI	Yell.	86.2			
		FI	Yell.	82.8	570	0.91	2.15
	4	FI	Yell.	85.8			
		FI	Yell.	84.4			
		FI	Yell.	83.9			
		FI	Yell.-Gre.	36.7			
		FI	Yell.-Gre.	32.3			
	5	FI	Yell.-Gre.	34.6	568	0.59	1.60
		FI	Yell.-Gre.	53.8			
	6	FI	Yell.	73.4	566	0.71	1.83
		FI	Yell.	70.2			
		FI	Yell.	80.1	568	0.84	2.04
	7	FI	Yell.	74.3			
		FI	Yell.	78.3			
	1	FI	Yell.	76.3			
		FI	Yell.	79.1	567	0.82	1.92
		FI	Yell.	88.1			
		FI	Yell.	87.8			
		FI	Yell.	84.4			
	2	FI	Yell.	84.4			
		FI	Yell.	85.3			
3426		FI	Yell.	85.4			
		FI	Yell.	82.4			
	3	FI	Yell.-Gre.	80.9	511	0.42	1.20
		FI	Gre.	89.5	512	0.40	1.13
	4	FI	Gre.	89.1	509	0.43	1.13
		FI	Gre.	90.3	510	0.43	1.15
		FI	Gre.	88.3	512	0.47	1.18
		FI	Yell.-Gre.	88.3			
		FI	Yell.-Gre.	76.8			
		FI	Yell.-Gre.	75.5			
	1	FI	Yell.-Gre.	75.5			
		FI	Yell.-Gre.	83.6			
		FI	Yell.-Gre.	71.7			
3432		FI	Yell.-Gre.	71.7			
		FI	Gre.	91.7			
		FI	Gre.	84.6			
	2	FI	Gre.	88.8			
		FI	Gre.	85.8			
		FI	Gre.	84.6			
		FI	Gre.	84.6			

	FI	Gre.	83.3			
	FI	Gre.	93.4	509	0.43	1.13
3	FI	Gre.	83.2			
	FI	Gre.	86.9			
	FI	Yell.-Gre.	84.6			
	FI	Yell.-Gre.	95.8	514	0.54	1.37
4	FI	Yell.-Gre.	86.4			
	FI	Yell.-Gre.	80.6			
	FI	Yell.-Gre.	80.6			
	FI	Yell.-Gre.	88			
	FI	Yell.-Gre.	93.8			
	FI	Yell.-Gre.	95.9			
	FI	Yell.-Gre.	92	514	0.49	1.31
	FI	Yell.-Gre.	97.3			
	FI	Yell.-Gre.	96.9			
5	FI	Yell.-Gre.	94.5			
	FI	Yell.-Gre.	95.3			
	FI	Yell.-Gre.	99.9			
	FI	Yell.-Gre.	95.3			
	FI	Yell.-Gre.	97.4			
	FI	Yell.-Gre.	96.2			
	FI	Yell.-Gre.	97.4			
	FI	Yell.-Gre.	97.4			
	FI	Yell.-Gre.	93.8			
6	FI	Gre.	80.3	516	0.39	1.13
	FI	Gre.	80.3			
	FI	Yell.-Gre.	89.1	566	0.59	1.58
	FI	Yell.-Gre.	91.5	568	0.63	1.66
7	FI	Yell.-Gre.	90.8			
	FI	Yell.-Gre.	94.5	568	0.58	1.54
	FI	Yell.-Gre.	91.1	567	0.62	1.62
	AI		142.4/-22.7			
	AI		142.4/-23.5			
	AI		134.1/-23.3			
	AI		140.2/-23.8			
	AI		125.2/-22.7			
8	AI		125.2/-21.9			
	AI		139.5/-22.1			
	FI	Yell.-Gre.	111.3			
	FI	Yell.-Gre.	111.3			
	FI	Yell.-Gre.	85.2			
	FI	Yell.-Gre.	89.6			
	FI	Yell.-Gre.	107.3			

		FI	Yell.-Gre.	96.8			
		FI	Yell.-Gre.	97.2			
	9	FI	Yell.-Gre.	106.5			
		FI	Yell.-Gre.	95.3			
		FI	Yell.-Gre.	100.3			
		FI	Yell.-Gre.	88.6			
		FI	Yell.-Gre.	86.9			
		FI	Yell.-Gre.	93.4			
	10	FI	Yell.-Gre.	93.4			
		FI	Yell.-Gre.	91.8			
		FI	Yell.-Gre.	78.9			
		FI	Yell.-Gre.	89.1			
		FI	Yell.-Gre.	91.8			
	1	FI	Yell.-Gre.	74.8			
		FI	Gre.	81.3	509	0.35	1.03
		FI	Gre.	86.8			
	2	FI	Gre.	86.8			
		FI	Gre.	86.4			
3734.6		FI	Gre.	83.9			
		FI	Yell.-Gre.	87.6			
		FI	Yell.-Gre.	90.8			
	3	FI	Yell.-Gre.	90.4	510	0.45	1.13
		FI	Yell.-Gre.	87.3			
		FI	Yell.-Gre.	89.3			

Table DR3. Raman geothermometers of bitumen in the BPFVs from 3432.0 m

Sample	Position-D1 (cm^{-1})	FWHM-D1 (cm^{-1})	T (FWHM-D1) (°C)
Median Plane	1361.5	160.9	132.0
	1366.1	156.7	141.0
	1358.8	161.6	130.6
	1364.1	161.5	130.8
Primary bitumen inclusions	1353.1	158.7	136.7
	1349.2	160.4	133.2
	1351.1	156.9	140.6
	1345.9	157.5	139.4
	1356.4	158.5	137.2
	1360.3	149.4	156.8
	1357.7	152.1	151.0
	1353.8	153.1	148.8
	1358.4	149.2	157.2
	1360.1	149.5	156.7

Table DR4. The strata top depth, stratigraphic present thickness, begin ages, the missing erosion thickness and the heat flux of each formation of Well NY-1

Formation	**Begin age (Ma)**	**Top depth (m)**	**Present thickness (m)**	**Missing thickness (m)**	**Heat flux (mW/m^2)**
Q	2	0	300		69
Nm	5.1	300	751		71
Ng	14	1051	471		72.5
Erosion	24.6			-400	84.5
Ed	32.8	1522	564		85.5
Es^{1}	36.7	2086	212		86.5
Es^{2}	38.2	2298	196.5		87
$Es^{3\ \mathrm{upper}}$	38.6	2494.5	290.5		88
$Es^{3\ \mathrm{middle}}$	42	2785	403		87.5
$Es^{3\ \mathrm{lower}}$	43.7	3188	127.98		86.5
$Es^{4\ \mathrm{upper}}$	45	3315.98	222.02		85
$Es^{4\ \mathrm{below}}$	52	3538	200		84